(1) Initialize $\mathbb{W}^0 = \mathbb{B}^0 = 0$;
(2) Update $r^k = (c_1^k - I)^2 - (c_2^k - I)^2$;
(3) Solve $\Delta_{\mathcal{M}} \varphi^{k+1} = \frac{\mu}{\lambda} r^k + \operatorname{div}_{\mathcal{M}}(\mathbb{W}^k - \mathbb{B}^k)$, then project $0 \le \varphi^{k+1} \le 1$ as in (8.14);
(4) $\mathbb{W}^{k+1} = \operatorname{shrink}\big(\nabla_{\mathcal{M}} \varphi^{k+1} + \mathbb{B}^k, 1/\lambda\big)$;
(5) $\mathbb{B}^{k+1} = \mathbb{B}^k + \nabla_{\mathcal{M}} \varphi^{k+1} - \mathbb{W}^{k+1}$;
(6) $c_1^{k+1} = \int_{\Omega^+(\varphi^{k+1})} I \, \mathrm{d}s, \quad c_2^{k+1} = \int_{\Omega^-(\varphi^{k+1})} I \, \mathrm{d}s$;
(7) Repeat until convergence.

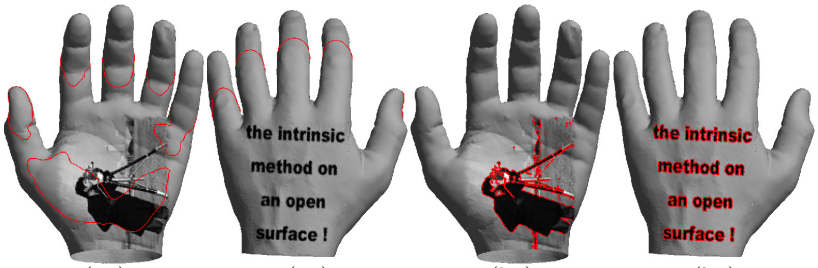

(a1) (a2) (b2) (b2)

Fig. 8.2 CCV segmentation results on a 58875 vertices a hand surface [Lai and Chan (2011)]. (a1), (a2) two views the image and the initial segmentation curve marked by the red contour. (b1), (b2) correspond to two views of the CCV segmentation result.

8.2 Computational optimal transport on manifolds

In Section 4.4, we have seen optimal transport (OT) on a flat domain. OT on manifolds provides a natural geometric framework to quantify distances between probability measures while respecting intrinsic curvature. When the underlying space $\mathcal{M}$ is a smooth compact Riemannian manifold with metric g, the dynamic formulation of OT generalizes the celebrated Benamou–Brenier formula from $\mathbb{R}^d$ to curved spaces [Lavenant *et al.* (2018)]. It can be further viewed as a special case of the potential mean-field game (MFG) functional studied in [Yu *et al.* (2023, 2024)], and solved efficiently by a projected (proximal) gradient descent scheme on triangular meshes. See Appendix C.2 for a quick introduction to the proximal gradient method.

Dynamic formulation of OT on manifolds. Let $\rho_0, \rho_1 \in \mathcal{P}(\mathcal{M})$ be two smooth probability densities. The L^2–Wasserstein distance on $(\mathcal{M}, g)$

can be written as the solution to a convex dynamic problem:

$$W_2^2(\rho_0,\rho_1) = \inf_{\rho,\, m} \int_0^1 \int_{\mathcal{M}} \frac{\|m(x,t)\|_g^2}{\rho(x,t)}\, \mathrm{d}V_g(x)\, \mathrm{d}t,$$
$$\text{s.t.}\ \ \partial_t \rho + \mathrm{Div}_{\mathcal{M}} m = 0,\ \rho(\cdot,0)=\rho_0,\ \rho(\cdot,1)=\rho_1. \tag{8.15}$$

Here $m(x,t) \in T_x\mathcal{M}$ represents the probability flux, and $\|m\|_g^2 = g_x(m,m)$ is the squared norm under metric g. The continuity equation evolves densities along vector fields tangent to $\mathcal{M}$, ensuring mass conservation.

Introducing a potential $\phi : \mathcal{M} \times [0,1] \to \mathbb{R}$ as Lagrange multiplier for the constraint, the corresponding Lagrangian reads

$$\mathcal{A}(\rho,m,\phi) = \int_0^1 \int_{\mathcal{M}} \frac{\|m\|_g^2}{2\rho} + \rho\, \partial_t \phi + \langle m, \nabla_{\mathcal{M}} \phi \rangle_g\, \mathrm{d}V_g\, \mathrm{d}t. \tag{8.16}$$

Stationarity in (ρ, m, ϕ) yields the manifold Hamilton–Jacobi–continuity system

$$\begin{cases} -\partial_t \phi + \frac{1}{2}\|\nabla_{\mathcal{M}}\phi\|_g^2 = 0, \\ \partial_t \rho - \mathrm{Div}_{\mathcal{M}}(\rho \nabla_{\mathcal{M}} \phi) = 0, \end{cases} \qquad \rho(\cdot,0)=\rho_0, \quad \rho(\cdot,1)=\rho_1. \tag{8.17}$$

This is the canonical form of the dynamic OT equations on manifolds, and a special case of the potential MFG system [Yu *et al.* (2023)] with zero interaction cost.

Variational formulation and convex functional. For a general convex Lagrangian $L(x,p)$, the dynamic OT cost generalizes to

$$\min_{\rho,m}\ \mathcal{J}(\rho,m) := \int_0^1 \int_{\mathcal{M}} \rho(x,t)\, L\Big(x, \frac{m(x,t)}{\rho(x,t)}\Big)\, \mathrm{d}V_g(x)\, \mathrm{d}t, \quad \text{s.t. } \partial_t \rho + \mathrm{Div}_{\mathcal{M}} m = 0. \tag{8.18}$$

With $L(x,p) = \frac{1}{2}\|p\|_g^2$, the optimality condition recovers (8.17). When additional interaction or terminal terms $F(\rho)$, $F_T(\rho(1))$ are added, one obtains the full potential MFG functional [Yu *et al.* (2023)]:

$$\mathcal{Y}(\rho,m) = \int_0^1 \int_{\mathcal{M}} \rho\, L\Big(x, \frac{m}{\rho}\Big)\, \mathrm{d}V_g\, \mathrm{d}t + \int_0^1 F(\rho(\cdot,t))\, \mathrm{d}t + F_T(\rho(\cdot,1)).$$

Projected (proximal) gradient descent on discrete manifolds. Discretizing $(\mathcal{M}, g)$ by a triangular mesh $\mathcal{M}_h$ with vertices $\{V_i\}$, local basis $\{e_i\}$, and intrinsic gradient/divergence operators $(\nabla_{\mathcal{M}_h}, \mathrm{Div}_{\mathcal{M}_h})$, we

denote by $P_i(t) \approx \rho(V_i, t)$ the discrete density and by $M_j(t) \approx m(T_j, t)$ the flux on triangle T_j. The semi-discrete dynamic OT problem becomes

$$\min_{P,M} \widetilde{\mathcal{J}}(P, M) = \sum_{k=1}^{n} \sum_{T_j} A_{T_j} P(T_j, t_k) L\Big(T_j, \frac{M(T_j, t_k)}{P(T_j, t_k)}\Big), \tag{8.19}$$

$$\text{s.t. } \partial_t P + \mathrm{Div}_{\mathcal{M}_h} M = 0, \;\; P(\cdot, 0) = P_0, \; P(\cdot, 1) = P_1. \tag{8.20}$$

To enforce the discrete continuity constraint, Yu–Lai–Li–Osher [Yu *et al.* (2023, 2024)] proposed a proximal gradient method:

$$(P^{\ell+\frac{1}{2}}, M^{\ell+\frac{1}{2}}) = (P^{\ell}, M^{\ell}) - \eta_\ell \nabla_{P,M} \widetilde{\mathcal{J}}(P^{\ell}, M^{\ell}), \tag{8.21}$$

$$(P^{\ell+1}, M^{\ell+1}) = \mathrm{proj}_{\mathcal{C}(P_0,P_1)}(P^{\ell+\frac{1}{2}}, M^{\ell+\frac{1}{2}}), \tag{8.22}$$

where $\mathcal{C}(P_0, P_1)$ is the discrete constraint set ensuring $\partial_t P + \mathrm{Div}_{\mathcal{M}_h} M = 0$. The projection step is equivalent to minimizing

$$\min_{(P,M)\in\mathcal{C}(P_0,P_1)} \frac{1}{2}\|P - P^{\ell+\frac{1}{2}}\|_V^2 + \frac{1}{2}\|M - M^{\ell+\frac{1}{2}}\|_T^2, \tag{8.23}$$

whose first-order optimality condition introduces a dual potential ψ satisfying a discrete Poisson-type equation:

$$(-\partial_t \partial_t - \mathrm{Div}_{\mathcal{M}_h} \nabla_{\mathcal{M}_h})\, \psi = \partial_t P^{\ell+\frac{1}{2}} + \mathrm{Div}_{\mathcal{M}_h} M^{\ell+\frac{1}{2}}. \tag{8.24}$$

Then the projected variables are updated via

$$P^{\ell+1} = P^{\ell+\frac{1}{2}} + \partial_t \psi, \qquad M^{\ell+1} = M^{\ell+\frac{1}{2}} + \nabla_{\mathcal{M}_h} \psi. \tag{8.25}$$

The linear operator in (8.24) can be pre-factored, and the iteration preserves both mass and positivity (with a safeguard $P^{\ell+1} \leftarrow \max(P^{\ell+1}, \varepsilon)$).

Algorithm 2 Projected gradient method for OT on triangular meshes

1: Initialize $P^{(0)}, M^{(0)}$ satisfying $P(\cdot, 0) = P_0$ and $P(\cdot, 1) = P_1$.
2: **for** $\ell = 0, 1, 2, \ldots$ **do**
3: Gradient step: $(P^{\ell+\frac{1}{2}}, M^{\ell+\frac{1}{2}}) = (P^{\ell}, M^{\ell}) - \eta_\ell \nabla_{P,M} \widetilde{\mathcal{J}}(P^{\ell}, M^{\ell})$.
4: Projection: solve $(\partial_t \partial_t^* - \mathrm{Div}_{\mathcal{M}_h} \nabla_{\mathcal{M}_h})\psi = \partial_t P^{\ell+\frac{1}{2}} + \mathrm{Div}_{\mathcal{M}_h} M^{\ell+\frac{1}{2}}$.
5: Update: $P^{\ell+1} = P^{\ell+\frac{1}{2}} + \partial_t \psi, \quad M^{\ell+1} = M^{\ell+\frac{1}{2}} + \nabla_{\mathcal{M}_h} \psi$.
6: Safeguard: $P^{\ell+1} \leftarrow \max(P^{\ell+1}, \varepsilon)$.
7: **end for**

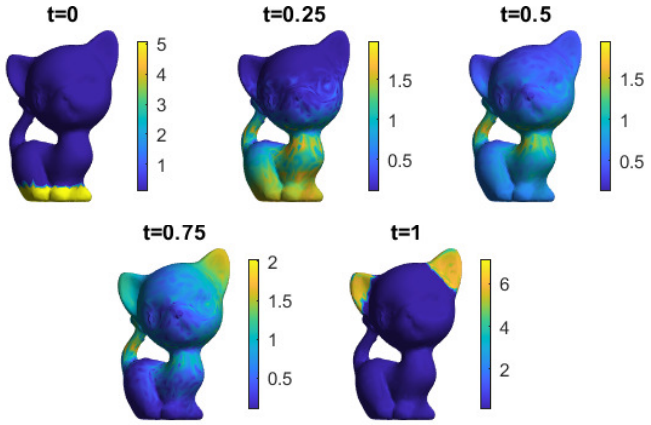

Fig. 8.3 Dynamical optimal transport on the kitten surface [Yu *et al.* (2023)].

8.3 Shape Analysis

Shape analysis seeks to extract, compare, and register geometric information from manifolds and surfaces in a coordinate-invariant manner. This section presents several representative methodologies built upon intrinsic operators such as the Laplace–Beltrami operator. The first part describes global conformal parameterization of genus zero surfaces, formulated as a constrained variational problem and efficiently solved by a manifold-based gradient descent method. The second part explains how spectral information from Laplace–Beltrami eigenfunctions can be used to derive skeletal structures that summarize global geometry. The final part develops intrinsic registration techniques for both nearly isometric and non-isometric shapes through Laplace–Beltrami eigenmaps.

8.3.1 *Conformal parameterization for Genus-0 surfaces*

Conformal parameterizations provide angle-preserving mappings from curved surfaces to simple parameter domains, enabling computations that respect intrinsic geometry. They are fundamental in computer vision, computer graphics, and medical imaging applications [Eck *et al.* (1995); Kanai *et al.* (1998); Levy *et al.* (2002); Alliez *et al.* (2002); Gu and Yau. (2002); Gu and Yau (2003); Gu *et al.* (2004); Springborn *et al.* (2008); Lui *et al.* (2008)]. For a compact, closed, genus-zero Riemannian surface $(\mathcal{M}, g)$, a global con-

formal parameterization onto the unit sphere (S^2, g_0) corresponds, up to Möbius transformations, to a harmonic map $\vec{F} = (f_1, f_2, f_3) : \mathcal{M} \to S^2$ that minimizes the Dirichlet energy under a spherical constraint [Schoen and Yau (1994); Jost (2008)]:

$$\begin{aligned} \min_{\vec{F}=(f_1,f_2,f_3)} \quad & \mathcal{E}(\vec{F}) = \frac{1}{2}\int_{\mathcal{M}} \big(\|\nabla_{\mathcal{M}} f_1\|^2 + \|\nabla_{\mathcal{M}} f_2\|^2 + \|\nabla_{\mathcal{M}} f_3\|^2\big)\, \mathrm{d}\mathcal{M}, \\ \text{subject to} \quad & \|\vec{F}(x)\|^2 = f_1^2(x) + f_2^2(x) + f_3^2(x) = 1, \quad \forall x \in \mathcal{M}. \end{aligned} \tag{8.26}$$

Unlike optimization problems in Euclidean space, where the objective can be decreased along straight-line search directions such as the negative gradient, optimization on a curved manifold requires motion constrained to the manifold itself. A natural choice for such motion is the geodesic, the intrinsic analogue of a straight line and the path of shortest length between two points on the manifold. Alternatively, iterative projection methods descend along straight directions and then project the intermediate results back to the constraint manifold. Both strategies are widely studied in optimization on manifolds [Absil *et al.* (2008)]. Since at each $x \in \mathcal{M}$, the constraint $\|\vec{F}(x)\| = 1$ defines a unit sphere, an efficient scheme can be designed using a sphere-geodesic descent approach [Lai *et al.* (2013b)], following the framework introduced in [Wen and Yin (2013)]. This method admits the use of acceleration techniques such as Barzilai–Borwein step selection and nonmonotone line search, while maintaining global convergence.

Constraint-preserving update. The constraint in (8.26) defines a manifold of unit-length vector fields, which can be regarded as a special case of the Stiefel manifold. The corresponding optimization can be viewed as a projected gradient method constrained to this manifold [Lai *et al.* (2013b)]. The Lagrangian associated with (8.26) is

$$\mathcal{L}(\vec{F}, \lambda) = \mathcal{E}(\vec{F}) - \frac{1}{2}\int_{\mathcal{M}} \lambda(x)\big(\|\vec{F}(x)\|^2 - 1\big)\, \mathrm{d}\mathcal{M},$$

where λ acts as a Lagrange multiplier enforcing the pointwise unit-norm condition. The first-order optimality conditions are

$$\begin{cases} H - \lambda \vec{F} = 0, \\ \|\vec{F}(x)\| = 1, \quad \forall x \in \mathcal{M}, \end{cases} \tag{8.27}$$

where $H = \nabla_{\vec{F}} \mathcal{E}(\vec{F}) = -(\Delta_{\mathcal{M}} f_1, \Delta_{\mathcal{M}} f_2, \Delta_{\mathcal{M}} f_3)$ is the Fréchet derivative of $\mathcal{E}(\vec{F})$, and $\Delta_{\mathcal{M}}$ is the Laplace–Beltrami operator. Applying the linear

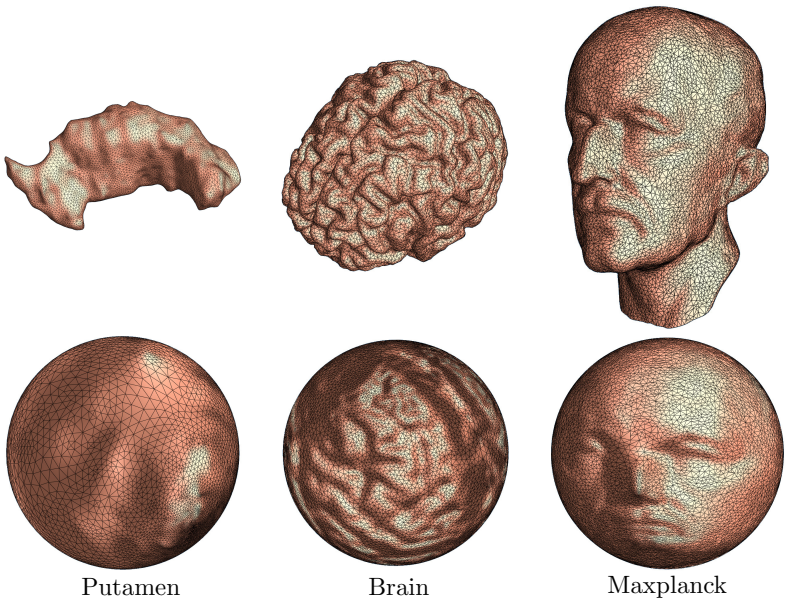

Fig. 8.4 First row: three input surfaces; Second row: the resulting conformal maps.

functional $\vec{F}^*$ to the first equation in (8.27) and using $\vec{F}^*\vec{F} = 1$ yields $\lambda = \vec{F}^* H = H^* \vec{F}$. Substitution into (8.27) gives

$$H - (\vec{F}^* H)\vec{F} = 0, \quad \text{equivalently,} \quad A\vec{F} = 0, \quad \text{with} \quad A := H\vec{F}^* - \vec{F}H^*.$$

The operator $A(x)$ is skew-symmetric for each $x \in \mathcal{M}$. Following [Wen and Yin (2013)], A defines a tangential search direction that preserves the unit-sphere constraint.

In Euclidean space, a standard gradient descent update is $\vec{Y}(x) = \vec{F}(x) - \tau A(x)\vec{F}(x)$, where $\tau > 0$ is a step size. However, this update generally violates the unit-norm constraint. To ensure $\|\vec{Y}(x)\| = 1$, an implicit update of the form

$$\vec{Y}(x) = \vec{F}(x) - \frac{\tau}{2} A(x)\big(\vec{F}(x) + \vec{Y}(x)\big)$$

is adopted. Solving for $\vec{Y}(x)$ yields

$$\vec{Y}(x) = \big(I + \tfrac{\tau}{2}A(x)\big)^{-1}\big(I - \tfrac{\tau}{2}A(x)\big)\vec{F}(x). \tag{8.28}$$

By the Cayley transformation, the operator $\big(I + \frac{\tau}{2}A(x)\big)^{-1}\big(I - \frac{\tau}{2}A(x)\big)$ is orthogonal, guaranteeing $\|\vec{Y}(x)\| = \|\vec{F}(x)\| = 1$. The step size τ can be adjusted adaptively through a line search scheme to ensure sufficient decrease of the objective. For example, a nonmonotone curvilinear search strategy can be adopted. We referred more details in [Wen and Yin (2013); Lai *et al.* (2013b)].

The method efficiently minimizes the harmonic energy under the spherical constraint and produces a globally consistent conformal parameterization for genus-zero surfaces.

It is worth to note that the procedure requires only a discretization of the Laplace–Beltrami operator. Hence, the same algorithmic framework applies to point clouds: using the corresponding discrete Laplace–Beltrami operator for point-sampled surfaces yields a fully analogous method for computing conformal parameterizations.

8.3.2 *Skeleton extraction from point clouds*

The first nontrivial eigenfunction of the Laplace–Beltrami operator encodes essential global geometric information of a surface and can be used to extract its topological structure. The approach introduced in [Shi *et al.* (2008); Liang *et al.* (2012)] constructs surface skeletons by forming the Reeb graph associated with this eigenfunction. Given a manifold $\mathcal{M}$ and its first nontrivial Laplace–Beltrami eigenfunction ϕ_1, the Reeb graph $R(\phi_1)$ is defined as the quotient space under the equivalence relation $x \sim y$ if and only if $\phi_1(x) = \phi_1(y)$ for $x, y \in \mathcal{M}$. The graph $R(\phi_1)$ captures the connectivity among the level sets of ϕ_1, providing a concise representation of the shape's global structure.

Algorithm (level-set barycenters).

(1) Compute ϕ_1 using the point-cloud LB eigenproblem (see Sec. 7.3.2 for MLS/graph discretizations).

(2) For a set of values $\{c_m\}$, extract approximate level contours $\{\phi_1 = c_m\}$: around each point p_i with $\phi_1(p_i) \in [c_m - \delta, c_m + \delta]$, solve

$$\min_{p \in \mathbb{R}^3} \ \|p - p_i\|^2 + \beta\big(\Phi_1(p) - c_m\big)^2,$$

where Φ_1 is the local polynomial fit of ϕ_1 (MLS), δ small, β large.

(3) For each level c_m, take the barycenter of the reconstructed contour as a skeleton node; connect nodes in order of c_m (or by nearest-neighbor in parameter c) to form the skeleton curve graph.

This procedure produces intuitive "backbone" summaries (e.g., figure-eight, armadillo, knot), showing that a single intrinsic eigenfunction can drive high-level structure recovery from unorganized points (see Fig. 8.5).

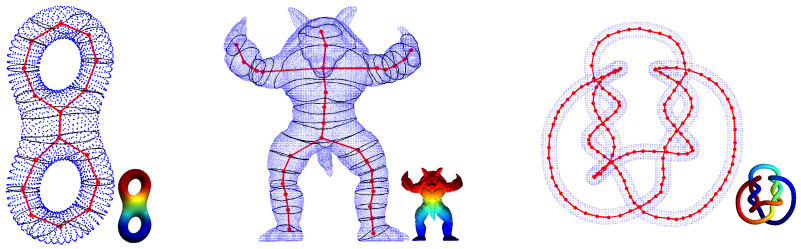

Fig. 8.5 Skeletons computed from the first nontrivial LB eigenfunction on point clouds. Blue: samples; black: level contours of ϕ_1; red: barycenters and skeleton connections [Liang *et al.* (2012)].

8.3.3 *Nonrigid manifolds registration via LB eigenmaps*

Intrinsic registration between two isometric or nearly isometric shapes is a central problem in geometry processing. For geometric shapes, the task is complicated by the absence of a global parameterization and by ambiguities arising from their embeddings in the ambient space $\mathbb{R}^D$. An effective strategy employs the Laplace–Beltrami eigenmap to construct intrinsic coordinates, resolves the eigenbasis ambiguity through an orthogonal alignment, and matches the resulting point distributions using a rotation invariant sliced Wasserstein distance.

Preliminaries: LB eigensystem and functional maps. For a closed Riemannian surface $(\mathcal{M}, g)$, the LB operator

$$\Delta_g \phi = \frac{1}{\sqrt{G}} \sum_{i=1}^{2} \frac{\partial}{\partial x_i} \Big(\sqrt{G} \sum_{j=1}^{2} g^{ij} \frac{\partial \phi}{\partial x_j} \Big), \qquad G = \det(g_{ij}), \tag{8.29}$$

is self-adjoint and elliptic, with spectrum $0 = \lambda_0 < \lambda_1 \leq \lambda_2 \leq \cdots$ and orthonormal eigenfunctions $\{\phi_i\}_{i \geq 0}$:

$$-\Delta_g \phi_i = \lambda_i \phi_i, \qquad \int_{\mathcal{M}} \phi_i \phi_j \, \mathrm{dvol}_g = \delta_{ij}.$$

The LB basis generalizes Fourier modes and is invariant under isometries. The resulting eigenpairs are intrinsic and stable under small metric perturbations [Chavel (1984); Jost (2008)]. Generic eigenfunctions are

Morse functions [Uhlenbeck (1976)], which support topological characterization through Morse theory [Milnor (1963)], and they provide global descriptors widely used in geometric comparison and retrieval [Rustamov (2007); Sun *et al.* (2009); Bronstein and Kokkinos (2010); Lai *et al.* (2010)]. Laplace–Beltrami based representations have become fundamental in surface analysis, medical shape correspondence, and manifold learning [Reuter (2010); Vallet and Levyvy (2008); Raviv *et al.* (2011); Bronstein *et al.* (2010); Lai *et al.* (2010); Shi *et al.* (2012); Lai and Zhao (2017)].

Nearly isometric registration Let $(\mathcal{M}, g_{\mathcal{M}})$ and $(\mathcal{N}, g_{\mathcal{N}})$ be d-dimensional Riemannian manifolds sampled by point clouds. Denote their first n nontrivial LB eigenpairs by $\Phi_n = \{(\lambda_k, \phi_k)\}_{k=1}^n$ and $\Psi_n = \{(\eta_k, \psi_k)\}_{k=1}^n$. The LB eigenmap $\iota_{\mathcal{M}}^n : \mathcal{M} \to \mathbb{R}^n$ is

$$\iota_{\mathcal{M}}^n(u) = \Big(\lambda_1^{-d/4}\phi_1(u), \dots, \lambda_n^{-d/4}\phi_n(u)\Big), \tag{8.30}$$

$$\iota_{\mathcal{N}}^n(v) = \Big(\eta_1^{-d/4}\psi_1(v), \dots, \eta_n^{-d/4}\psi_n(v)\Big). \tag{8.31}$$

which is intrinsic and stable to isometries [Bérard *et al.* (1994); Lai *et al.* (2010)]. However, eigenfunctions are defined up to sign and, within multiplicity blocks, up to orthogonal mixing; hence LB embeddings are only defined up to $R \in O(n)$.

Let $P \in \mathbb{R}^{\ell_P \times n}$ and $Q \in \mathbb{R}^{\ell_Q \times n}$ collect the row-wise embeddings of samples $\{u_i\}_{i=1}^{\ell_P} \subset \mathcal{M}$ and $\{v_j\}_{j=1}^{\ell_Q} \subset \mathcal{N}$, with discrete probability weights $\mu^P \in \mathbb{R}_+^{\ell_P}$ and $\mu^Q \in \mathbb{R}_+^{\ell_Q}$ (e.g., uniform). We align (PR, μ^P) and (Q, μ^Q) *in distribution* by optimal transport, while optimizing over $R \in O(n)$ to remove eigenbasis ambiguity [Lai and Zhao (2017)]:

$$\mathrm{RSWD}\big((P,\mu^P),(Q,\mu^Q)\big)^2 = \min_{R\in O(n)} \int_{S^{n-1}} \min_{\sigma^{\theta,R}\in \mathrm{ADM}(\mu^P_{\theta,R},\mu^Q_\theta)} \sum_{i,j} \sigma_{ij}^{\theta,R} \left(p_i R\theta^\top - q_j\theta^\top\right)^2 \mathrm{d}\theta, \tag{8.32}$$

where $\mu_{\theta,R}^P$ and μ_θ^Q are the pushforward 1D measures induced by projections $p_i \mapsto p_i R\theta^\top$, $q_j \mapsto q_j\theta^\top$. Each inner 1D OT is solved by sorting in $O(m \log m)$, giving scalability [Bonneel *et al.* (2015); Lai and Zhao (2017)]. The optimization over R handles sign/multiplicity/ordering ambiguities in the LB basis. (Under a natural equivalence that identifies point sets up to permutations and $O(n)$, RSWD defines a distance; see [Lai and Zhao (2017)].)

In practice, approximate (8.32) by Monte Carlo directions $\{\theta_t\}_{t=1}^T$:

(1) **Initialize.** $R \leftarrow I_n$ (or from coarse scale; see multiscale below).

(2) **Project.** For each t, compute $a^{(t)} = PR\theta_t^\top \in \mathbb{R}^{\ell_P}$ and $b^{(t)} = Q\theta_t^\top \in \mathbb{R}^{\ell_Q}$.
(3) **1D OT.** Sort $a^{(t)}$ and $b^{(t)}$ and compute the optimal coupling $\sigma^{(t)}$ matching their cumulative masses (linear-time after sorting).
(4) **Update** R**.** Minimize

$$\min_{R\in O(n)} \frac{1}{T}\sum_{t=1}^{T}\sum_{i,j}\sigma_{ij}^{(t)}\left(p_i R\theta_t^\top - q_j\theta_t^\top\right)^2 \quad\Longleftrightarrow\quad \max_{R\in O(n)} \operatorname{tr}\Big(R^\top H\Big),$$

with $H = \frac{1}{T}\sum_t P^\top D^{(t)} Q\,\theta_t\theta_t^\top$ and $D^{(t)}$ a sparse matrix encoding $\sigma^{(t)}$ (derived from pairings after sorting). Solve by orthogonal Procrustes: $H = U\Sigma V^\top$, $R \leftarrow UV^\top$.
(5) **Repeat** 2–4 until convergence of the RSWD objective or of R.

LB eigenmaps are naturally multiscale: small n captures coarse/global structure, larger n adds detail. We thus register progressively:

$$n_1 < n_2 < \cdots < n_L, \qquad R_k \text{ initialized by } R_{k-1} \text{ (padded to } n_k).$$

This improves robustness, speed, and accuracy.

Remarks. (i) If shapes are nearly isometric, the optimal R captures only sign/permutation within multiplicity blocks; RSWD reduces to standard functional-map alignment. (ii) Weights μ^P, μ^Q can reflect sampling density or area elements (via local PCA/MLS). (iii) The method integrates seamlessly with additional descriptors by concatenating to the LB embedding prior to RSWD.

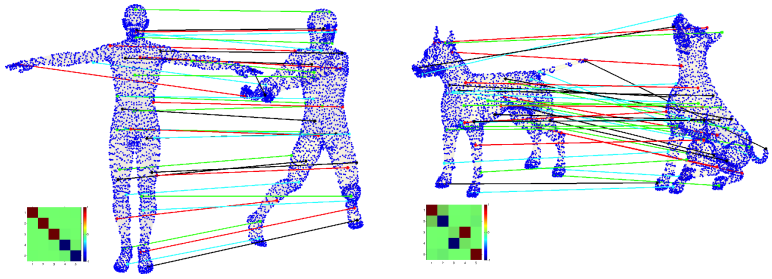

Fig. 8.6 Registration using the first 5 nontrivial LB modes ($n = 5$). We plot aligned embeddings and the resulting 5×5 orthogonal matrices $R^\star$; uniform weights $\mu^P = \mu^Q = 1/N$.

Non-isometric registration via conformal basis alignment. For large nonrigid deformations, classical spectral descriptors may misalign. A conformal deformation rescales the metric by a positive factor $g \mapsto \tilde{g} = w^2 g$. On genus-0 surfaces, conformal equivalence implies that alignment can be mediated by a scalar weight $w > 0$ on the target. The LB eigensystem on $(\mathcal{M}_2, \tilde{g})$ is equivalent to a *weighted* problem on $(\mathcal{M}_2, g_2)$:

$$-\Delta_{g_2}\psi = \lambda\, w^2 \psi, \qquad \int_{\mathcal{M}_2} \psi_i \psi_j\, w^2 \,\mathrm{dvol}_{g_2} = \delta_{ij}. \tag{8.33}$$

This suggests coupling a conformal weight with a weighted LB basis so that *feature coefficients* match across shapes [Schonsheck *et al.* (2021)].

Let $\Phi = \{\phi_i\}_{i=1}^N$ be fixed on $\mathcal{M}_1$ and $\Psi = \{\psi_i\}_{i=1}^N$ be a weighted-orthonormal basis on $(\mathcal{M}_2, w^2 g_2)$. Given paired features $F = \{f_\ell\}_{\ell=1}^k$ and $G = \{g_\ell\}_{\ell=1}^k$, consider

$$\min_{w>0,\ \Psi} \ \tfrac{r_1}{2} \Big\| \underbrace{\Big(\int_{\mathcal{M}_1} f_\ell \phi_i \,\mathrm{dvol}_{g_1}\Big)}_{\langle F, \Phi\rangle_{g_1}} - \underbrace{\Big(\int_{\mathcal{M}_2} g_\ell \psi_i\, w^2 \,\mathrm{dvol}_{g_2}\Big)}_{\langle G, \Psi\rangle_{w^2 g_2}} \Big\|_F^2 \ + \ \tfrac{r_2}{2} \textstyle\sum_{i=1}^N \int_{\mathcal{M}_2} \|\nabla_{g_2} \psi_i\|^2 \,\mathrm{dvol}_{g_2}$$

$$\text{s.t.} \qquad \textstyle\int_{\mathcal{M}_2} \psi_i \psi_j\, w^2 \,\mathrm{dvol}_{g_2} = \delta_{ij}. \tag{8.34}$$

The first term aligns feature *coefficients*; the second enforces near-harmonicity of Ψ on $(\mathcal{M}_2, w^2 g_2)$.

Optimization outline. A practical scheme alternates [Schonsheck *et al.* (2021)]:

(1) *Basis update* (w fixed): minimize (8.34) w.r.t. Ψ under the weighted orthonormality constraint. Use a splitting method (e.g., ADMM): a quadratic "alignment + smoothing" subproblem for Ψ, followed by substituting $Q \leftarrow M^{1/2}(w)\Psi$ onto the weighted-orthonormal Stiefel set, where $M(w)$ is the w^2-weighted mass matrix.
(2) *Weight update* (Ψ fixed): parameterize $w^2 = \exp(\eta)$ and solve a regularized least-squares problem for η (optionally with Laplacian smoothing), then renormalize $M(w)$ and repeat.

This alternating procedure progressively reduces coefficient mismatch while preserving weighted orthonormality, yielding robust alignments under large conformal distortions.

After the final basis is obtained, a point-to-point correspondence between the two surfaces can be established by comparing the values of the corresponding basis functions. This procedure follows the principle of the

functional map framework introduced in [Ovsjanikov *et al.* (2012)], applied here to the newly constructed basis. The correspondence is determined by performing a nearest-neighbor search (with $K = 1$) between the rows of Φ and Ψ, which involves comparing n points in a k-dimensional space. This approach provides a more efficient and accurate correspondence than direct delta-function matching.

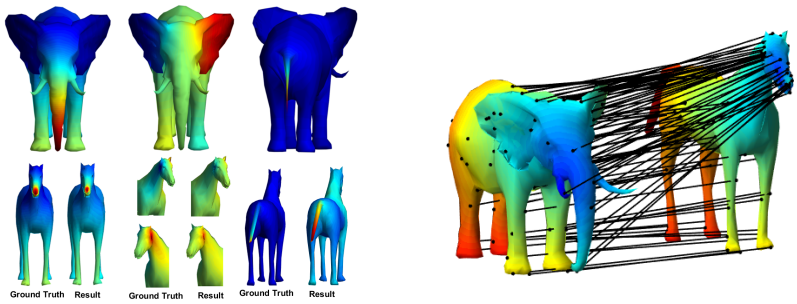

Fig. 8.7 Top left: 9th, 11th and 44th natural LB eigenfunctions on source. Bottom left: results and ground truth. Right: visualization of point-to-point map and texture transfer [Schonsheck *et al.* (2021)].

8.4 Committor problem on point clouds

The committor function describes the probability that a stochastic trajectory first reaches a prescribed product region before a reactant region. It provides a quantitative characterization of transition pathways in molecular and chemical systems. The local mesh method introduced in [Lai *et al.* (2013a); Lai and Lu (2018)] can be adapted to compute the committor on point clouds using only sampled data, even when samples concentrate near transition manifolds.

Model. Consider the overdamped Langevin dynamics

$$\mathrm{d}X_t = -\nabla U(X_t)\,\mathrm{d}t + \sqrt{2\beta^{-1}}\,\mathrm{d}W_t, \tag{8.35}$$

where $U : \Omega \to \mathbb{R}$ is a potential, $\beta = (k_B T)^{-1}$ is the inverse temperature, and W_t is a standard Wiener process. For disjoint reactant and product